The Astrophysical Journal, 959:2 (10pp), 2023 December 10 https://doi.org/10.3847/1538-4357/ad05c0

Bridging the Gap between Cosmic Dawn and Reionization Favors Models Dominated by Faint Galaxies

Ankita Bera[1,2,3], Sultan Hassan[2,4,5,14], Aaron Smith[6,7], Renyue Cen[8,9,10], Enrico Garaldi[11], Rahul Kannan[6,12], and Mark Vogelsberger[13]
[1] School of Astrophysics, Presidency University, 86/1 College Street, Kolkata 700073, India; ankita1.rs@presiuniv.ac.in
[2] Center for Computational Astrophysics, Flatiron Institute, 162 5th Ave., New York, NY 10010, USA
[3] Department of Astronomy, University of Maryland, College Park, MD 20742, USA
[4] Center for Cosmology and Particle Physics, Department of Physics, New York University, 726 Broadway, New York, NY 10003, USA
[5] Department of Physics & Astronomy, University of the Western Cape, Cape Town 7535, South Africa
[6] Center for Astrophysics | Harvard & Smithsonian, 60 Garden Street, Cambridge, MA 02138, USA
[7] Department of Physics, The University of Texas at Dallas, Richardson, TX 75080, USA
[8] Department of Astrophysical Sciences, Princeton University, Peyton Hall, Princeton, NJ 08544, USA
[9] Institute for Advanced Study in Physics, Zhejiang University, Hangzhou 310027, People's Republic of China
[10] Institute of Astronomy, Zhejiang University, Hangzhou 310027, People's Republic of China
[11] Max-Planck Institute for Astrophysics, Karl-Schwarzschild-Str. 1, D-85741 Garching, Germany
[12] Department of Physics and Astronomy, York University, 4700 Keele Street, Toronto, Ontario MJ3 1P3, Canada
[13] Department of Physics, Massachusetts Institute of Technology, Cambridge, MA 02139, USA
Received 2022 October 7; revised 2023 October 12; accepted 2023 October 19; published 2023 November 28

Abstract

It has been claimed that traditional models struggle to explain the tentative detection of the 21 cm absorption trough centered at $z \sim 17$ measured by the EDGES collaboration. On the other hand, it has been shown that the EDGES results are consistent with an extrapolation of a declining UV luminosity density, following a simple power law of deep Hubble Space Telescope observations of $4 < z < 9$ galaxies. We here explore the conditions by which the EDGES detection is consistent with current reionization and post-reionization observations, including the neutral hydrogen fraction at $z \sim 6$–8, Thomson-scattering optical depth, and ionizing emissivity at $z \sim 5$. By coupling a physically motivated source model derived from radiative transfer hydrodynamic simulations of reionization to a Markov Chain Monte Carlo sampler, we find that it is entirely possible to reconcile existing high-redshift (cosmic dawn) and low-redshift (reionization) constraints. In particular, we find that high contributions from low-mass halos along with high photon escape fractions are required to simultaneously reproduce cosmic dawn and reionization constraints. Our analysis further confirms that low-mass galaxies produce a flatter emissivity evolution, which leads to an earlier onset of reionization with a gradual and longer duration, resulting in a higher optical depth. While the models dominated by faint galaxies successfully reproduce the measured globally averaged quantities over the first one billion years, they underestimate the late redshift-instantaneous measurements in efficiently star-forming and massive systems. We show that our (simple) physically motivated semianalytical prescription produces results that are consistent with the (sophisticated) state-of-the-art THESAN radiation-magnetohydrodynamic simulation of the reionization.

Unified Astronomy Thesaurus concepts: Reionization (1383); Galaxies (573)

1. Introduction

Some of the most important but least explored phases in the evolutionary history of our Universe are the epochs of cosmic dawn and reionization. The ignition of the first luminous cosmic structures, either stars or active galactic nuclei (AGNs), marks the beginning of cosmic dawn. These sources of first light gradually and inhomogeneously transformed the intergalactic medium (IGM) from being predominately filled with cold neutral hydrogen gas to a warm ionized plasma (for reviews, see, e.g., Barkana & Loeb 2001; Wise 2019; Robertson 2022).

Currently, there are several observational global constraints on reionization at $z \gtrsim 5$, including measurements of the volume-averaged neutral hydrogen fraction of the IGM using different techniques such as the evolution in Lyα and Lyβ forests (Fan et al. 2001; White et al. 2003; McGreer et al. 2015) and Lyα emitters (Ouchi et al. 2010; Zheng et al. 2011; Mesinger et al. 2014; Sobacchi & Mesinger 2015; Mason et al. 2019), the optical depth to Thomson scattering of cosmic microwave background (CMB) photons as measured by Planck Collaboration et al. (2020), and the ionizing emissivity constraints as compiled by Becker & Bolton (2013). However, more stringent constraints are expected from the 21 cm measurements, which will play a crucial role in mapping the H I distribution to trace the large-scale structure. Experiments such as the Low Frequency Array (LOFAR; Patil et al. 2017), the Hydrogen Epoch of Reionization Array (HERA; DeBoer et al. 2017), and the Square Kilometre Array (SKA; Mellema et al. 2013) are devoted to detecting the 21 cm fluctuations during reionization.

Complementary constraints on cosmic dawn come from the measurements of the 21 cm global signal at $z > 15$. These include the Experiment to Detect the Global Reionization

[14] NHFP Hubble Fellow.

Signature (EDGES; Bowman et al. 2018), the Shaped Antenna measurement of the background Radio Spectrum (SARAS; Singh et al. 2022), the Large-Aperture Experiment to Detect the Dark Ages (LEDA; Price et al. 2018), and the Radio Experiment for the Analysis of Cosmic Hydrogen (REACH; De & Acedo 2019; de Lera Acedo et al. 2022). At this epoch, the controversial EDGES detection (Bowman et al. 2018) of a flattened absorption profile in the sky-averaged radio spectrum, centered at 78 MHz with an amplitude of 0.5 K, provides a tentative constraint on the 21 cm global signal during cosmic dawn. Explaining the detection of this deep absorption trough requires additional physics that can lead, for instance, to a higher star formation rate (SFR) density (Mirocha & Furlanetto 2019; Mebane et al. 2020; Mittal & Kulkarni 2022) or to new exotic physics during cosmic dawn, such as the interaction between dark matter and baryons (see, e.g., Barkana 2018; Muñoz et al. 2018; Slatyer & Wu 2018), and the excess radio background (e.g., Ewall-Wice et al. 2018; Feng & Holder 2018; Fraser et al. 2018; Pospelov et al. 2018; Fialkov & Barkana 2019; Ewall-Wice et al. 2020).

Inferred from the EDGES signal, Madau (2018) have derived a constraint on the early star formation and showed that it is consistent with an extrapolation of UV measurements at lower redshifts ($4 < z < 9$). While many theoretical (see, e.g., Hills et al. 2018; Bradley et al. 2019; Singh & Subrahmanyan 2019; Sims & Pober 2020) and observational works (see, e.g., Singh et al. 2022) have suggested that the profile measured by EDGES has no astrophysical origin, it is timely to understand the implications that this detection might have on cosmic dawn and reionization, in particular, whether additional constraints can be placed on the role of faint and bright galaxies during these epochs if the measurement holds. In light of the recent successful launch of the James Webb Space Telescope (JWST) and the growing observational efforts to detect the 21 cm signal during cosmic dawn, many high-redshift constraints are expected, and hence it is currently a scientific priority to ask what is required to bridge the gap between cosmic dawn and reionization.

Here we use a semianalytical approach coupled with a Markov Chain Monte Carlo (MCMC) sampler to explore the range of scenarios and models that are most consistent with the combined constraints from cosmic dawn and reionization. Because all considered constraints are globally averaged quantities, a semianalytical approach is sufficiently accurate while also being much faster than using reionization simulations, for which numerical limitations in the resolution, box size, subgrid physics, and radiation transport prescriptions complicate the interpretability and feasibility of parameter explorations (e.g., Mesinger et al. 2011; Hassan et al. 2017; Vogelsberger et al. 2020; Wu et al. 2021). To obtain insights into the role of faint and bright galaxies, we use a physically motivated source model for the ionization rate ($R_{\rm ion}$) that was derived from radiative transfer simulations (Finlator et al. 2015; Hassan et al. 2016). This parameterization assumes a nonlinear relation between the ionization rate and the halo mass $R_{\rm ion} \propto M_h^{C+1}$, where $C = 0$ corresponds to a linear relation, as is typically assumed in many seminumerical models of reionization via the efficiency parameter (Mesinger et al. 2011). In addition to the C parameter, we aim to constrain the most debated parameter in reionization models, namely, the escape fraction of ionizing photons $f_{\rm esc}$. Harnessing the MCMC framework, our aim is to explore the joint C–$f_{\rm esc}$ parameter space to determine the range of models that naturally reproduce the combined constraints from reionization and cosmic dawn. Finally, we aim to study the implications of these constraints for the galaxy evolution during these early formation epochs.

This paper is organized as follows: we describe our empirical source model in Section 2 and calibrate it to cosmic dawn (EDGES) constraints in Section 3. We then constrain our model to several reionization observables in Section 4, jointly to both cosmic dawn and reionization in Section 5, and we finally present our concluding remarks in Section 6.

We assume a flat ΛCDM cosmology throughout this paper with the cosmological parameters obtained from the recent Planck Collaboration et al. (2020) measurements, i.e., $\Omega_\Lambda = 0.69$, $\Omega_{\rm m} = 0.31$, $\Omega_{\rm b} = 0.049$, and the Hubble parameter $H_0 = 67.66\ {\rm km\ s^{-1}\ Mpc^{-1}}$.

2. Source Model

In this section, we discuss the details of the source model considered in this work. To study the role of different populations of galaxies, we considered a physically motivated source model that was derived in Hassan et al. (2016) from the radiative transfer simulations of reionization described in Finlator et al. (2018). In this model, the ionization rate $R_{\rm ion}$ is parameterized as a function of halo mass (M_h) and redshift (z). The mass dependence of $R_{\rm ion}$ is analogous to the Schechter function, which can be characterized as a power law on the bright end and as an exponential cutoff on the faint end. The redshift dependence follows a simple power law. This parameterization of $R_{\rm ion}$ accounts for the nonlinear dependence on halo mass, which can be expressed as follows:

$$\frac{R_{\rm ion}}{M_h} = A(1+z)^D \left(\frac{M_h}{B}\right)^C \exp\left[-\left(\frac{M_h}{B}\right)^{-3}\right], \qquad (1)$$

where A, B, C, and D are free parameters, and their best-fit values were obtained by calibration to radiative transfer simulations. We refer to Hassan et al. (2016) for more details about the derivation of this model. We now discuss the physical meaning of these free parameters. Parameter A acts as an amplitude of $R_{\rm ion}$, which scales the ionizing emissivity over the entire halo mass range at a given redshift by the same amount. Parameter B determines the minimum halo mass, which can be thought of as the quenching mass scale due to feedback from star formation and photoionization heating. Parameter C quantifies the slope of the $R_{\rm ion}$–M_h relation, which controls the contribution of different mass scales to the total emissivity. Last, parameter D accounts for the redshift dependence of the ionization rate for a given halo mass.

Having defined our source model $R_{\rm ion}$, we adopt the Sheth & Tormen (1999) halo mass function ($\frac{dn}{dM}$), which provides the number density of halos per unit halo mass, to compute the cosmic evolution of the global quantities governing reionization and comic dawn. In this work, we consider the halo mass range from 10^5 to $10^{15}\ M_\odot$ to account for the contribution from all source populations, including the faintest halos.

The most interesting parameters of this source model are parameters B and C because they allow us to draw conclusions about the role of different source populations during cosmic dawn and reionization. Therefore, we set the amplitude $A = 10^{40}\ M_\odot^{-1} {\rm s}^{-1}$ and redshift index $D = 2.28$, following the

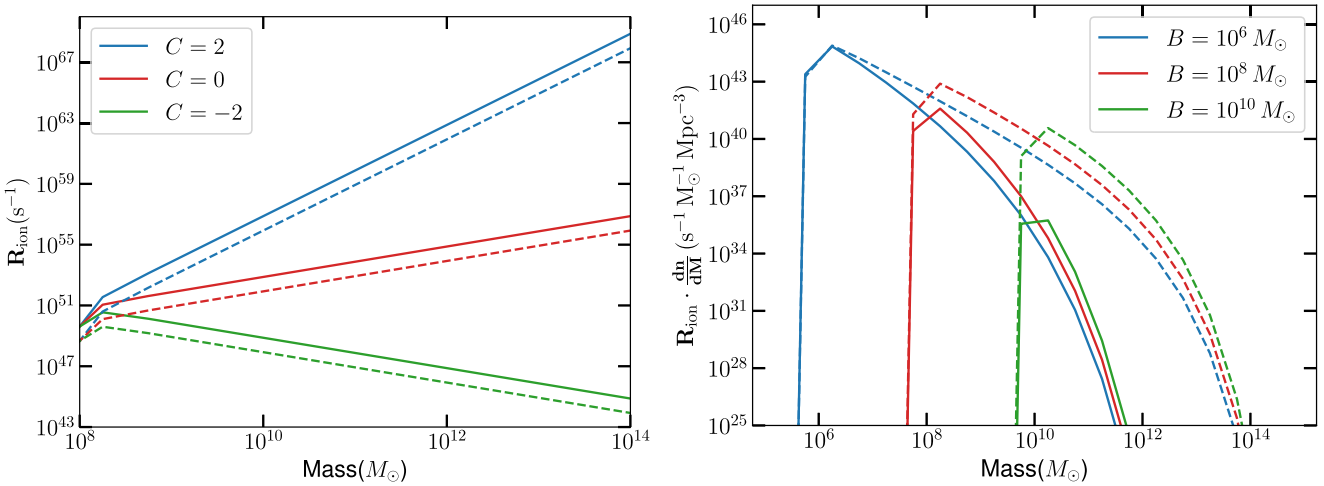

Figure 1. Left panel: The ionization rates for different C values at $z \sim 17$ (solid) and $z \sim 6$ (dashed) while fixing other parameters to values of $A = 10^{40}\,M_\odot^{-1}{\rm s}^{-1}$, $B = 10^8\,M_\odot$, and $D = 2.28$ as derived from radiative transfer simulations (Hassan et al. 2016). This shows that positive and negative C correspond to higher ionization rate efficiencies from massive and low-mass halos, respectively. Right panel: The ionization rates multiplied by the Sheth–Tormen halo mass function for different values of B while keeping the other parameters fixed at $A = 10^{40}\,M_\odot^{-1}{\rm s}^{-1}$, $C = -0.5$, and $D = 2.28$. Parameter B represents the minimum halo mass ($M_{h,\rm min}$) considered in the model.

calibration to radiative transfer simulations (for more details, see Hassan et al. 2016)[15] throughout. To illustrate how the source model parameters (B and C) affect the $R_{\rm ion}$–M_h relation, we show in Figure 1 several $R_{\rm ion}$ models with different values of C and B at cosmic dawn ($z \sim 17$, solid) and reionization ($z \sim 6$, dashed). As parameter C scales the ionization rate ($R_{\rm ion}$) as a function of halo mass following $R_{\rm ion} \propto M_h^{C+1}$, $C = 0$ (red curves) corresponds to a linear relation, shown in the left panel of Figure 1. However, in the case of $C = 2$ (blue curves), the emissivity increases with halo mass and hence favors a relatively larger contribution from more massive halos than from low-mass halos, and vice versa for the case of $C = -2$ (green curves), where reionization is dominated by low-mass halos. While this depends on the photon escape fraction, under the assumption of a mass-independent escape fraction, the intrinsic $R_{\rm ion}$ increases by several orders of magnitude from low- to high-mass halos, as shown in Figure 1. In the right panel, we show the impact of varying the B parameter, which sets the minimum halo mass scale.

3. Source Model Calibration to Cosmic Dawn (EDGES) Constraints

Our goal is to find the possible range of models that can reproduce the existing observational constraints during cosmic dawn and reionization. To do this, we first calibrate our source model parameters (C, B) to the intrinsic UV luminosity density ($\rho_{\rm UV}$) inferred from the EDGES signal in the redshift range $z \sim 5$–20, where the function $\log_{10}[\rho_{\rm UV}/({\rm erg\ s^{-1}\ Mpc^{-3}\ Hz^{-1}})] = (26.30 \pm 0.12) + (-0.130 \pm 0.018)(z-6)$ is the best fit as compiled by Madau (2018).

Using our source model, we compute the UV luminosity density as follows. First, the ionization rate $R_{\rm ion}$ (Equation (1)) can be converted into a star formation rate (SFR) by accounting for a stellar metallicity-dependent parameterization of the ionizing photon flux $Q_{\rm ion}$, following

$$\mathrm{SFR} = R_{\rm ion}(M_h, z)/Q_{\rm ion}(Z). \quad (2)$$

The subsolar metallicity-dependent parameterization is provided by Finlator et al. (2011),

$$\log Q_{\rm ion}(Z) = 0.639(-\log Z)^{1/3} + 52.62 - 0.182, \quad (3)$$

where $Q_{\rm ion}$ is in units of ${\rm s}^{-1}\,(M_\odot\ {\rm yr}^{-1})^{-1}$. This form of $Q_{\rm ion}$ is consistent with the equilibrium values measured by Schaerer (2003) assuming a Chabrier (2003) initial mass function (IMF). We also adopt the Madau & Fragos (2017) redshift evolution of the mass-weighted metallicity (Z), given by

$$\log(Z/Z_\odot) = 0.153 - 0.074\,z^{1.34}. \quad (4)$$

The SFR can then be written in terms of the UV luminosity density $L_{\rm UV}$ (Kennicutt 1998; Madau et al. 1998) as follows:

$$\mathrm{SFR}[M_\odot\ {\rm yr}^{-1}] = 1.25 \times 10^{-28} L_{\rm UV}[{\rm ergs\ s^{-1}\ Hz^{-1}}]. \quad (5)$$

The global $\rho_{\rm UV}$ is obtained by integrating $\int L_{\rm UV}\frac{dn}{dm}dm$ over the entire mass range at different redshifts.

We now constrain our source model parameters (B and C) to the Madau (2018) UV luminosity evolution using EMCEE, which is an affine-invariant ensemble sampler for MCMC (Foreman-Mackey et al. 2013). We assume a flat prior in the range $\log(B/M_\odot) \in [5, 10]$ and $C \in [-5, 5]$. Our task is to find the range of models that minimizes the following multivariate χ^2 distribution:

$$\chi^2 \equiv \sum_z \frac{(\rho_{\rm UV,model}(z) - \rho_{\rm UV,obs}(z))^2}{2(\sigma_{\rho_{\rm UV,obs}}(z))^2}. \quad (6)$$

In the left panel of Figure 2, we show several posterior distributions of parameters B and C by considering different epochs, namely, cosmic dawn ($z > 16$, green), reionization ($z < 10$, red), and the combination of cosmic dawn plus reionization ($z \sim 5$–20, blue). The dark and light shaded contours correspond to 1σ and 2σ levels, respectively. From the one-dimensional probability distribution function (PDF) of parameter B (i.e., $M_{h,\rm min}$), it is clear that the minimum halo mass or the mass cutoff varies between $\sim 10^{6-8}\,M_\odot$. It is also

[15] We have varied the A and D parameters to reproduce several observations using MCMC and found similar values. Hence, fixing these parameters has a minimal impact on the results.

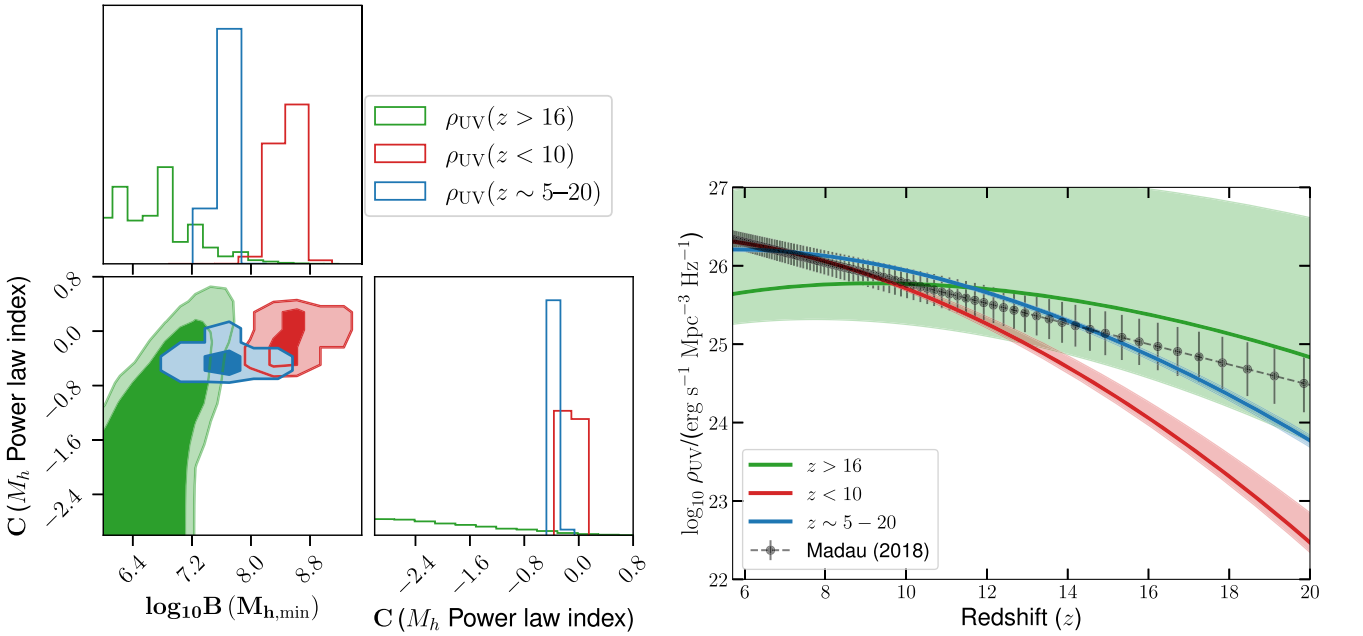

Figure 2. Left panel: Several posterior distributions derived using the UV luminosity density (Madau 2018), including constraints for three different redshift ranges, namely $z > 16$ (representing cosmic dawn only, green), $z < 10$ (during reionization only, red), and $z \sim 5$–20 (cosmic dawn and reionization, by combining the full redshift range, blue). Right panel: Comparison between several UV luminosity densities calculated from $R_{\rm ion}$ with the inferred parameter values using MCMC. This figure indicates that fitting to $z > 16$ favors more negative C values, which implies stronger contributions from low-mass (faint) galaxies.

evident that calibrating the model to reproduce higher-z $\rho_{\rm UV}$ constraints ($z > 16$) favors models with lower mass cutoffs ($\sim 10^6\,M_\odot$), and vice versa. Likewise, a more negative C is preferred to match with higher-z constraints. As discussed before, the negative value of C and the low value of B both suggest that the low-mass (faint) halos play an important role in reproducing the extrapolated $\rho_{\rm UV}$ constraints. Overall, using $\rho_{\rm UV}$ measurements in the entire redshift range ($z \sim 5$–20) provides much tighter posterior contours than constraining to either $z > 16$ or $z < 10$. This is mainly due to the number of redshift bins used in each case. Because the time duration in the redshift range of $z = 16$–20 is shorter than that of $z = 5$–20 or $z = 5$–10, more redshift bins exist in the latter than the former, and hence, more constraining power is expected. Each of the best-fit values with 1σ errors is provided in Table 1 for the three scenarios. In the right panel of Figure 2, we compare the $\rho_{\rm UV}$ evolution predictions from these three models with the Madau (2018) $\rho_{\rm UV}$ evolution. The shaded areas show the 1σ confidence levels that are obtained by translating the parameter 1σ levels from Table 1 into constraints on $\rho_{\rm UV}$. All models are within the 1σ level of the $\rho_{\rm UV}$ constraints over the relevant redshift ranges. This figure clearly demonstrates that a stronger contribution from low-mass halos is required to reproduce the $\rho_{\rm UV}$ constraints inferred from EDGES during cosmic dawn (green curve). This is shown in the right panel of Figure 1, where the maximum halo mass during reionization ($z = 6$, dashed) is about two orders of magnitude higher than during cosmic dawn ($z = 17$, solid).

Because our aim is to bridge the gap between cosmic dawn and reionization, we fix parameter B (i.e., $M_{h,\rm min}$) to the value obtained by calibrating the source model to the $\rho_{\rm UV}$ constraints over the entire redshift range ($z = 5$–20). At the same time, we keep the halo mass power-law index parameter (C) as a free parameter to explore its correlations with the escape fraction of ionizing photons ($f_{\rm esc}$), and to test whether similar values can be derived by adding reionization constraints, which we discuss next.

Table 1
Best-fit Values of the Mass Cutoff (B) and Power Dependence on Halo Mass (C)

Parameters	$z > 16$	$z < 10$	$z \sim 5-20$
$\log_{10} B$	$6.34^{+0.69}_{-0.80}$	$8.49^{+0.16}_{-0.17}$	$7.67^{+0.07}_{-0.15}$
C	$-6.43^{+3.78}_{-9.0}$	$-0.11^{+0.04}_{-0.05}$	$-0.34^{+0.03}_{-0.03}$

Note. The other model parameters are fixed to values obtained by fitting to radiative transfer simulations ($A = 10^{40}\,M_\odot^{-1}{\rm s}^{-1}$ and $D = 2.28$; see Hassan et al. 2016).

4. Constraining the Source Model for Key Reionization Observables

We consider three key reionization observables to place constraints on our source model parameters, namely the ionizing emissivity, the neutral fraction in the IGM, and the Thomson optical depth to the CMB. In addition to the halo-mass power-law index parameter (C), we also vary the fraction of ionizing photons ($f_{\rm esc}$) that successfully escape the remaining neutral hydrogen clumps and dust extinction in the interstellar medium (ISM) and circumgalactic medium (CGM) to contribute to the IGM ionization process. In this work, we assume a constant $f_{\rm esc}$ at all redshifts because our $R_{\rm ion}$ function (Equation (1)) already accounts for redshift and mass dependence. We assume a flat prior in the range $f_{\rm esc} \in [0, 1]$ and $C \in [-10, 10]$, and combine different data using a multivariate Gaussian likelihood (similar to Equation (6)).

4.1. The Ionizing Emissivity, $\dot{N}_{\rm ion}$

The integrated emission rate density of ionizing photons, or ionizing emissivity ($\dot{N}_{\rm ion}$), is a measure of the total number of

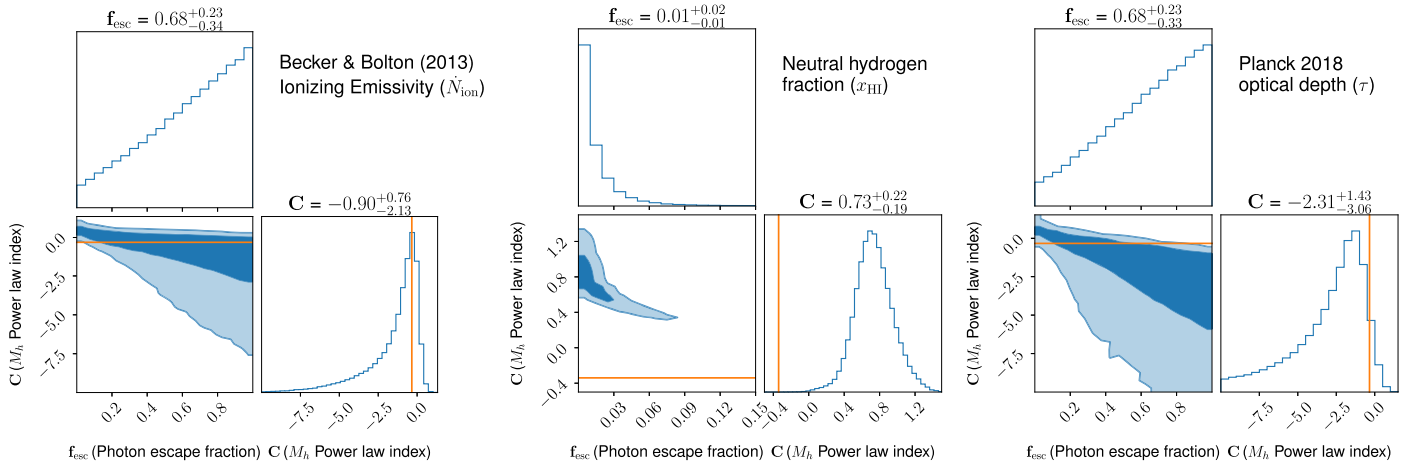

Figure 3. Posterior distributions for the escape fraction of ionizing photons f_{esc} and power-law index C as constrained by the ionizing emissivity ($\dot{N}_{ion}$; left), IGM neutral fraction ($x_{H\,I}$; middle), and Thomson optical depth (τ; right). The orange line in each plot denotes the value of parameter C obtained in Table 1 for $z \sim 5$–20 for reference. The emissivity and optical depth do not provide tight constraints on our parameters because of the large uncertainties. The IGM neutral fraction measurements provide tighter constraints on our parameters and favor models with low f_{esc} and positive C values, suggesting that reionization is driven by massive (bright) galaxies.

ionizing photons per second per volume that escape from all ionizing sources to the IGM. In our case, the ionizing emissivity is related to the ionization rate (R_{ion}) as follows:

$$\dot{N}_{ion}[s^{-1}\,Mpc^{-3}] = f_{esc}\int R_{ion}(M_h, z)\frac{dn}{dM_h}dM_h, \quad (7)$$

where $\frac{dn}{dM_h}$ is the Sheth & Tormen (1999) differential halo mass function, which gives the number density of halos in the mass range of M and $M + dM$ per unit comoving volume. We constrain our source model parameters (C, f_{esc}) to the Becker & Bolton (2013) ionizing emissivity constraint at $z = 4.75$ of $\log_{10}[\dot{N}_{ion}/(10^{51}\,\text{photons s}^{-1}\,\text{Mpc}^{-3})] = -0.014^{+0.454}_{-0.355}$.

In the left panel of Figure 3, we show the f_{esc}–C joint posterior distribution constrained to match the ionizing emissivity measurement. This shows that the $\dot{N}_{ion}$ measurement alone cannot place a tight constraint on these parameters due to the large uncertainty. However, $\dot{N}_{ion}$ data favor models with higher f_{esc} and more negative C, leading to a stronger contribution from low-mass halos. Similar parameter constraints were found in our earlier work on calibrating seminumerical simulations to reionization observables (Hassan et al. 2017). The best-fit value of C parameter obtained in the previous section for $z \sim 5$–20 is also within the 1σ level, as shown by the horizontal orange line in Figure 3.

4.2. The IGM Neutral Fraction, $x_{H\,I}$

We compute the reionization history from our models as follows. The rate of change in the ionized fraction of intergalactic hydrogen ($x_{H\,II}$) is given by Madau et al. (1999),

$$\frac{dx_{H\,II}}{dt} = \frac{\dot{N}_{ion}}{\bar{n}_H} - \frac{x_{H\,II}}{\bar{t}_{rec}}. \quad (8)$$

The first term describes the growth as a ratio of the comoving ionizing emissivity ($\dot{N}_{ion}$) and volume-averaged comoving number density of intergalactic hydrogen $\bar{n}_H$, which is given by

$$\bar{n}_H = X\Omega_{b,0}\rho_{crit,0}/m_H. \quad (9)$$

Here, X is the cosmic hydrogen mass fraction (0.76), $\rho_{crit,0}$ is the present-day critical density, and m_H is the mass of a hydrogen atom. The second term models the sink of ionizing photons, where the recombination timescale for the IGM is given by

$$t_{rec} = [C_{H\,II}\alpha_A(1 + \chi)\bar{n}_H(1 + z)^3]^{-1}. \quad (10)$$

Here, $C_{H\,II}$ is the redshift-dependent clumping factor, which we adopt from Pawlik et al. (2015). This clumping factor accounts for the overall density fluctuations in the ionized medium, which boosts the recombination rate by a factor up to $\sim$5 near the end of reionization. It is predominantly contributed by the ionized medium in the vicinity of halos. $\chi = Y/4X$, where Y denotes the helium mass fraction (0.24). Here, α_A is the case A recombination coefficient ($4.2 \times 10^{-13}\,\text{cm}^3\,\text{s}^{-1}$), corresponding to a temperature of 10^4 K (Kaurov & Gnedin 2014). After computing the reionization history, we now constrain our source model parameters to the IGM neutral fraction measurements given in Table 2.

In the middle panel of Figure 3, we show the parameter constraints given the above combination of IGM neutral fraction data. The $x_{H\,I}$ data provide the tightest constraints, with a clear tendency for the data to favor models with low f_{esc} and a positive parameter C. This implies that massive (bright) galaxy-dominated models are preferred. The low f_{esc} value (1%) found here is a consequence of the nonlinear relation between R_{ion} and M_h^C through parameter C, where an anticorrelation between f_{esc} and C is observed. However, we find that the resulting C value is not within the range reported in Table 1, and hence, we combine different constraints in the next section to understand the degeneracy between f_{esc} and C. Using the same source model in seminumerical simulations of reionization, we have previously found that $f_{esc} = 4\%$ is sufficient to match the reionization observations (Hassan et al. 2016), which is still within the 2σ level of the current constraints based on updated observational data. We also find a lower f_{esc} value because our current analysis includes contributions from the wider halo mass range of $10^{5-15}\,M_\odot$ as opposed to $10^{8-12}\,M_\odot$ in Hassan et al. (2016). Low f_{esc} values like this have been favored in several works (Gnedin et al. 2008; Wise et al. 2014; Ma et al. 2015; Carucci & Corasaniti 2019; Rosdahl et al. 2022; Yeh et al. 2023).

Table 2
IGM Neutral Hydrogen Fraction Measurements

Redshift(z)	Constraints	Observables	References
5.9	$\leqslant 0.06 \pm 0.05$	Lyα and Ly-β forest dark fraction	McGreer et al. (2015)
7.0	$0.59^{+0.11}_{-0.15}$	Lyα EW distribution	Mason et al. (2018)
7.09	0.48 ± 0.26	QSO damping wings	Davies et al. (2018)
7.5	$0.21^{+0.17}_{-0.19}$		Greig et al. (2019)
7.54	$0.60^{+0.20}_{-0.23}$		Davies et al. (2018)
7.6	$0.88^{+0.05}_{-0.10}$	Lyman-break galaxies emitting Lyα	Hoag et al. (2019)

However, it is worth noting that in this work, we consider a constant $f_{\rm esc}$, and defer exploring the impact of assuming a mass- and/or redshift-dependent $f_{\rm esc}$ to future works.

4.3. Thomson Optical Depth, τ

The optical depth is a measure of the scattering of CMB photons by free electrons produced by reionization. Given a reionization history, it is straightforward to obtain the Thomson scattering optical depth (τ) as follows:

$$\tau = \int_0^\infty dz \frac{c(1+z)^2}{H(z)} \sigma_T \bar{n}_{\rm H} [x_{\rm H\,II}(1+\chi) + \chi\, x_{\rm He\,III}], \quad (11)$$

where σ_T is the Thomson cross section, and c is the speed of light. The integrated optical depth is calculated considering hydrogen and helium reionization following Madau & Haardt (2015). This optical depth can also be used to constrain the timing of reionization, where lower or higher τ corresponds to later or earlier reionization redshifts, respectively.

In the right panel of Figure 3, we show the resulting posterior distribution of fitting to the measured value of $\tau = 0.054 \pm 0.007$ from Planck Collaboration et al. (2020). Similar to the case with $\dot{N}_{\rm ion}$ (left panel), τ alone does not place tight constraints on our parameters because of the large uncertainty that is consistent with a broad range of reionization histories. The tendency to favor models with high $f_{\rm esc}$ and negative C is also seen. However, allowing a much more negative C as compared to values derived from $\dot{N}_{\rm ion}$ data suggests that a stronger contribution from low-mass halos is needed to reproduce the Planck Collaboration et al. (2020) τ in our model. The constraints placed on parameter C using $\rho_{\rm UV}$ data for $z \sim 5$–20 are consistent with the constraints obtained by calibrating to Planck Collaboration et al. (2020) τ at the 1–2σ level, as shown by the horizontal orange line.

5. Constraining the Source Model to Reionization and Cosmic Dawn

We now turn our attention to the main goal of this work, which is to determine the range of models that can successfully reproduce reionization and cosmic dawn constraints. For reionization, we consider all measurements from the previous section that include the $\dot{N}_{\rm ion}$, $x_{\rm H\,I}$, and τ data. As mentioned earlier, the only existing constraint during cosmic dawn comes from the EDGES detection at $z \sim 17$, from which Madau (2018) have been able to place constraints on the UV luminosity density $\rho_{\rm UV}$ (see Section 3). We now constrain our source model to reionization-only constraints ($\dot{N}_{\rm ion} + x_{\rm H\,I} + \tau$), and to combined reionization and cosmic dawn constraints ($\dot{N}_{\rm ion} + x_{\rm H\,I} + \tau + \rho_{\rm UV}$). We refer to the former as EoR($\dot{N}_{\rm ion} + x_{\rm H\,I} + \tau$) and to the latter as CD(EDGES) + EoR($\dot{N}_{\rm ion} + x_{\rm H\,I} + \tau$). We compare the two resulting posterior distributions in Figure 4. Blue and red correspond to reionization only (EoR) and cosmic dawn plus reionization (CD+EoR), respectively. In both cases, combined observations place tight constraints on our parameters, but in different parts of the parameter space. Compared with Figure 3, the reionization combined observations (blue, EoR) are mainly driven by the reionization history measurements ($x_{\rm H\,I}$). This shows that a constraint to reionization observations favors models with low $f_{\rm esc}$ and positive C, indicating that massive galaxies play a major role in driving reionization. On the other hand, a constraint to both reionization and cosmic dawn observations (red, CD+EoR) favors models with high $f_{\rm esc}$ and negative C, suggesting that low-mass galaxies play a dominant role in bridging the gap between these two epochs. This is represented by the diagonal shift from the blue to the red contours when the cosmic dawn constraint ($\rho_{\rm UV}$ from EDGES)

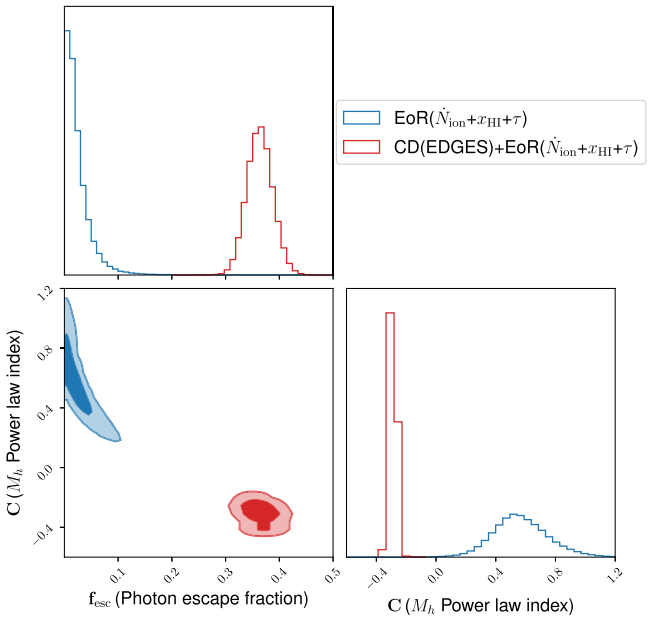

Figure 4. Comparison between the combined constraints from reioniztion, EoR ($\dot{N}_{\rm ion}$, $x_{\rm H\,I}$, τ) in blue, and by adding cosmic dawn to reionization, CD ($\rho_{\rm UV}$ from EDGES) + EoR ($\dot{N}_{\rm ion}$, $x_{\rm H\,I}$, τ) in red. The dark and light shaded contours correspond to the 1$\sigma$and 2σ levels, respectively. This demonstrates that adding cosmic dawn constraints shifts the contours toward higher $f_{\rm esc}$ and negative C parameters. This suggests that low-mass (faint) galaxies play a major role in bridging the gap between cosmic dawn and reionization.

Table 3
Best-fit Values of the Photon Escape Fraction (f_{esc}) and the Power Dependence on Halo Mass (C)

Parameters	Constraints			Reionization (EoR)	Cosmic Dawn (CD)+Reionization (EoR)
	$\dot{N}_{ion}(z = 4.75)$	$x_{H\,I}(z = 5.9\text{–}7.6)$	τ	$\dot{N}_{ion} + x_{H\,I} + \tau$	$\rho_{UV} + \dot{N}_{ion} + x_{H\,I} + \tau$
f_{esc}	$0.68^{+0.23}_{-0.34}$	$0.01^{+0.02}_{-0.01}$	$0.68^{+0.22}_{-0.33}$	$0.02^{+0.02}_{-0.01}$	$0.36^{+0.02}_{-0.02}$
C	$-0.90^{+0.76}_{-2.13}$	$0.73^{+0.22}_{-0.19}$	$-2.31^{+1.43}_{-3.06}$	$0.56^{+0.19}_{-0.17}$	$-0.29^{+0.02}_{-0.02}$

Note. Parameters A and D are fixed to values obtained by calibration to radiative transfer simulations ($A = 10^{40}\,M_{\odot}^{-1}\mathrm{s}^{-1}$, $D = 2.28$; see Hassan et al. 2016) and B to the derived value from fitting to ρ_{UV} in the entire redshift range $z \sim 5$–20 ($\log(B/M_{\odot}) = 7.67$; see Table 1).

is added to the likelihood. All best-fit parameters and their 1σ confidence intervals are listed in Table 3.

In Figure 5 we present predictions based on these best-fit parameters for the ionizing emissivity (top), reionization history (middle), and cumulative optical depth (bottom) from the EoR (blue) and CD+EoR (red) models. The shaded regions reflect the 1σ uncertainty of the derived constraints (see Table 3). In each panel, we add the relevant observations used in the MCMC analysis. We then compare our predictions with results from the THESAN project (Garaldi et al. 2022; Kannan et al. 2022; Smith et al. 2022), which provides a suite of radiation-magnetohydrodynamic simulations that self-consistently evolve reionization on large scales ($L_{box} = 95.5$ cMpc) and resolve most of the ionizing sources that cause it ($m_{gas} = 5.82 \times 10^5 M_{\odot}$) with galaxy formation physics based on the state-of-the-art IllustrisTNG model (Vogelsberger et al. 2014a, 2014b; Marinacci et al. 2018; Naiman et al. 2018; Nelson et al. 2018; Pillepich et al. 2018; Springel et al. 2018). Specifically, we compare with the THESAN-HIGH and THESAN-LOW simulation runs (dotted curves), where reionization is mainly driven by high- and low-mass galaxies, respectively.

In the top panel of Figure 5, we compare our predictions for the ionizing emissivity evolution with the THESAN runs (based on the ray-tracing escape fraction calculations of Yeh et al. 2023) and with the measurements of Becker & Bolton (2013). Our models (EoR and CD+EoR) and the different THESAN runs are consistent within the 1–2σ levels of the observations. The emissivity evolution in the EoR model (blue) gradually increases toward decreasing redshifts as more massive halos form. This is a consequence of the positive C value inferred by reionization observations, which leads to stronger contributions from massive halos. On the other hand, the CD+EoR model (red) infers a negative C value, which gives more weight to the low-mass halos. This results in a higher $\dot{N}_{ion}$ predicted by the CD+EoR model as compared to the EoR model predictions at high redshifts ($z \gtrsim 10$). As more massive halos form at lower redshifts ($z \lesssim 10$), the EoR model produces higher $\dot{N}_{ion}$ than the CD+EoR model, where the emissivity in the latter starts to decrease due to the negative C value. This leads to a flatter emissivity evolution in the CD+EoR model (red). In addition to observations, our different models produce emissivity histories that are consistent with the model predictions from the THESAN simulations. Our EoR and CD+EoR models show a similar emissivity evolution as the THESAN-HIGH and THESAN-LOW, respectively, because the models share similar assumptions.

In the middle panel of Figure 5, we compare the reionization history of our models and the THESAN runs against observationally inferred measurements. As with the emissivity, we see similar reionization histories between EoR/CD+EoR models and THESAN-HIGH/THESAN-LOW simulations, respectively. Reionization begins earlier in faint galaxy-dominated models (CD+EoR, THESAN-LOW) than in bright galaxy-dominated models (EoR, THESAN-HIGH) because faint (bright) galaxies are predominant (rare) at high redshift. Reionization is also more gradual (longer duration) in faint galaxy-dominated models, whereas bright galaxy-dominated scenarios yield a more sudden (shorter duration) neutral-to-ionized transition of the Universe. This earlier onset of reionization in the CD+EoR and THESAN-LOW models translates into a higher cumulative optical depth, as shown in the bottom panel of Figure 5, which is consistent within the 1–2σ levels with the Planck Collaboration et al. (2020) measurements. On the other hand, the sudden (late) reionization history in the massive galaxy-dominated models (EoR and THESAN-HIGH) produces a lower optical depth that is also consistent with the 1σ level of the data. In addition, our EoR model agrees with the late reionization models presented in Kulkarni et al. (2019), which reproduce the large-scale opacity fluctuations measurements (Becker et al. 2018).

To test whether our present models (EoR and EoR+CD) provide plausible predictions in terms of star formation, we calculate the star formation efficiency f_* using Equations (1) and (4) in Sun & Furlanetto (2016). In case of EoR model, we find that it is $\sim$10% at $M_h = 10^9\,M_{\odot}$ and then increases with halo mass. In contrast, the efficiency peaks at 1% for our CD+EoR model and then decreases with increasing halo mass because this model favors a greater contribution from faint galaxies. The f_* evolution in Sun & Furlanetto (2016) lies between the predicted f_* in our models. In particular, at a representative redshift $z \sim 8$ and at $M_h = 10^{10}\,M_{\odot}$, our EoR model predicts an efficiency of 40%, while the CD+EOR model predicts 0.5%, which brackets the Sun & Furlanetto (2016) model efficiency prediction of 3%. We furthermore compute the star formation timescales (t_{SF}) in our models using the approximate relation, $\mathrm{SFR} = f_* \frac{\Omega_b}{\Omega_m} \frac{M_h}{t_{SF}}$. We find that it increases/decreases with M_h in the EoR/EoR+CD models, respectively. For both of our models, the average t_{SF} is about $\sim$1 Gyr, consistent with commonly assumed values in traditional star formation models (e.g., Springel & Hernquist 2003). However, it is worth mentioning that our models differ from instantaneous star formation rate functions (SFRF) or UV luminosity functions (UVLF) at different redshifts. The solid blue and green lines in Figure 6 represent the SFRF predictions from our EoR and CD+EoR models at $z = 7$, while the dashed lines depict the same at $z = 6$. For instance, we find that our EoR model overestimates the SFR functions over the entire SFR range as compared to the Smit et al. (2012; at $z \sim 6$ and 7) and Bouwens et al. (2015; at $z \sim 8$) SFRFs, as shown in Figure 6. In contrast, our CD+EoR model underestimates the SFRFs in efficiently star-forming and massive systems. The SFRF data at $z = 8$ in violet are taken from Katsianis et al. (2017) and were calculated using the luminosity functions from

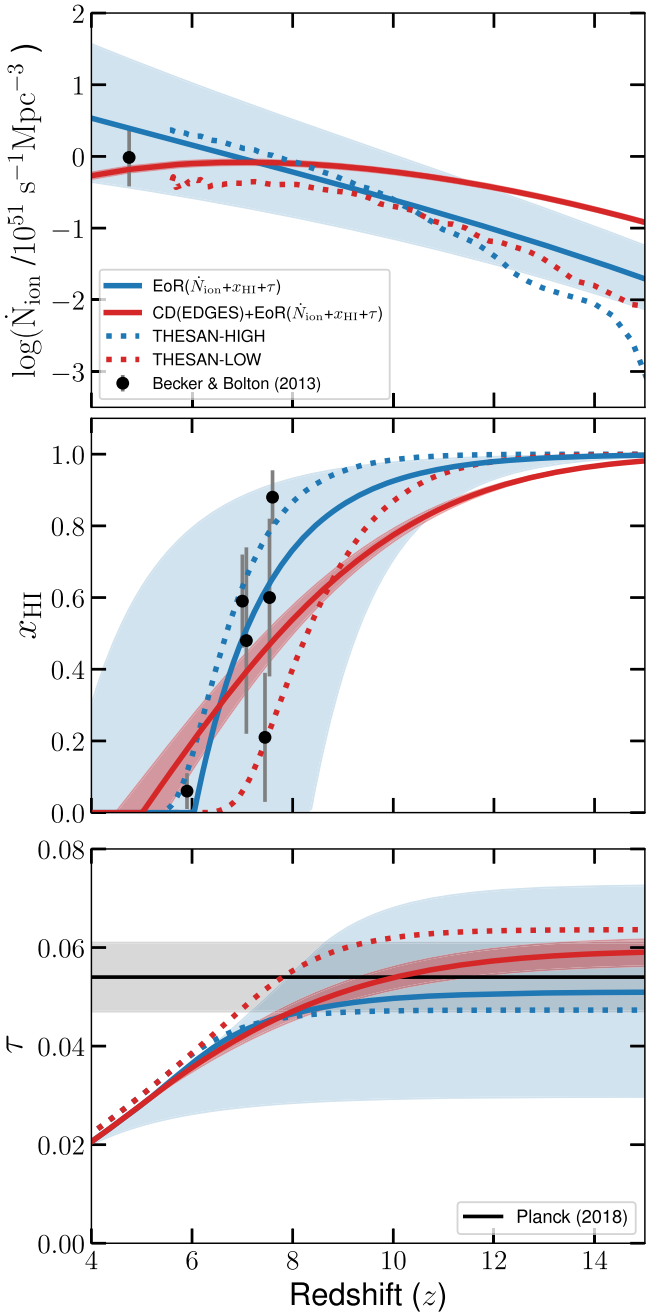

Figure 5. Top: Redshift evolution of the ionizing emissivity, $\dot{N}_{\rm ion}$, as predicted by our models, EoR (solid blue) and CD+EoR (solid red), along with the observational constraint by Becker & Bolton (2013). The dotted blue and red curves show the THESAN-HIGH and THESAN-LOW simulations, respectively. Middle: The neutral hydrogen fraction, $x_{\rm H\,I}$, as compared to the data listed in Section 4.2. Bottom: The Thomson optical depth, τ, as compared to the Planck Collaboration et al. (2020) measurement (black line) with 1σ uncertainty (gray shaded region). Massive galaxy-dominated models (blue) favor a gradually increasing emissivity, which in turn produces a later onset of reionization, a more sudden and shorter duration, and a lower optical depth. Faint galaxy-dominated models (red) favor a nearly flat emissivity evolution with the opposite characteristics.

Bouwens et al. (2015). Because our models are calibrated to the globally averaged quantities, we do not expect our models to reproduce detailed redshift-instantaneous observables. However, our CD+EoR model, which is calibrated to all observables, broadly agrees with the Madau & Dickinson (2014) cosmic SFR density at low redshifts. As demonstrated

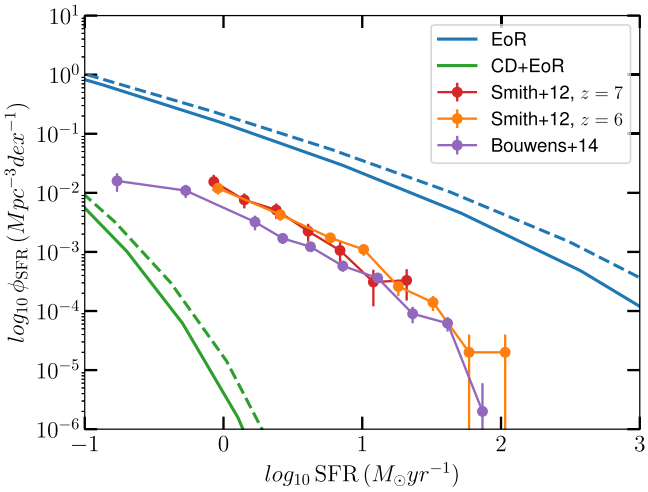

Figure 6. The SFR functions at $z=7$ obtained for the EoR model and for the CD+EoR model are plotted as solid blue and green curves, respectively. The dashed lines represent the same evaluated at $z=6$. The SFRFs from Smit et al. (2012; at $z\sim6$, 7) and Bouwens et al. (2015; at $z\sim8$) are plotted for comparison.

by the CD+EoR model, it is entirely possible to reconcile the different observational constraints from cosmic dawn to post-reionization using faint galaxy-dominated models of reionization, without the need to invoke new physics or exotic sources to explain the potential detection by EDGES.

6. Conclusions

We have presented a detailed analysis to explore the conditions by which the controversial EDGES detection (Bowman et al. 2018) is consistent with reionization and post-reionization measurements including the ionizing emissivity ($\dot{N}_{\rm ion}$), IGM neutral hydrogen fraction ($x_{\rm H\,I}$), and Thomson optical depth (τ) measurements. To account for the EDGES detection during cosmic dawn, we use the inferred constraint on the UV luminosity density ($\rho_{\rm UV}$) following Madau (2018), which is consistent with a simple extrapolation of deep HST observations of $4<z<9$ galaxies.

Based on a semianalytical framework of reionization with a physically motivated source model (Hassan et al. 2016) coupled with MCMC likelihood sampling, our key findings are as follows:

1. Calibrating our source model $R_{\rm ion}$ to cosmic dawn constraints ($\rho_{\rm UV}$ from EDGES) favors models with negative C values. This indicates that a stronger contribution from low-mass (faint) galaxies is required to reproduce the inferred $\rho_{\rm UV}$ constraints from EDGES (see Figure 2 and Table 1).
2. Constraining our source model $R_{\rm ion}$ to different reionization observables is mainly driven by the IGM neutral fraction measurements, where models with low $f_{\rm esc}$ and positive C values are favored. This suggests that massive (bright) galaxies play the main role in driving reionization (see Figures 3 and 4 and Table 3).
3. Further constraining our source model $R_{\rm ion}$ to both reionization ($\dot{N}_{\rm ion}+x_{\rm H\,I}+\tau$) and the cosmic dawn constraint ($\rho_{\rm UV}$ from EDGES) favors models with high $f_{\rm esc}$ and negative C values. This implies that low-mass (faint) galaxies play a crucial role in bridging the gap

between cosmic dawn and reionization (see Figure 4 and Table 3).

4. Massive (bright) galaxy-dominated models produce an increasing emissivity that results in a later onset of reionization, a more sudden and shorter reionization duration, and a lower optical depth (see Figure 5). Low-mass (faint) galaxy-dominated models result in a flatter emissivity evolution with the opposite reionization history characteristics.

It is worth mentioning several limitations to this work. First, the inferred $\rho_{\rm UV}$ values from EDGES compiled by Madau (2018) do not take the depth or shape of the detected profile into account, but the constraints are instead imposed by the required Wouthuysen-Field coupling strength on UV radiation backgrounds at the detection redshift. As mentioned in Madau (2018), accounting for the amplitude might require new physics, which in turn might alter our finding. We leave an accounting for the whole properties of the detected profile to future works. Second, we use a linear relation between the SFR and $L_{\rm UV}$ in the entire redshift range ($z = 5$–20), which has been derived from low redshift. This SFR–$L_{\rm UV}$ relation might not be linear at high redshift, and assuming a different form might change our results quantitatively. Third, due to the high degeneracies between the $R_{\rm ion}$ parameters, we have fixed the amplitude A and redshift dependence D to values found in Hassan et al. (2016) by calibrating to radiative transfer simulations of reionization. We confirmed the results when A is included as a free parameter and found approximately the same value as was obtained in Hassan et al. (2016). Parameter D might not be the same at different redshifts due to the evolution in galactic feedback. However, we have obtained our fit from radiative transfer simulations using data from $z = 6$ to 12, and it has been shown that the observed SFR function parameters show a weak dependence on redshift in Smit et al. (2012). Hence, we do not expect a qualitative change in our results if D is varied. Fourth, the quantitative results might be different if parameters A, B, and D were fixed to different values. Nevertheless, the qualitative result (high/low redshift data prefer models with more negative/positive C and higher/lower $f_{\rm esc}$, respectively) would be similar. Fifth, our models have been adjusted to match the globally averaged quantities. As a result, we observe that the EoR and CD+EoR model over- and underproduces the SFR functions (or equivalently, the UV luminosity functions), respectively. We leave it to future works to perform a detailed analysis to calibrate our models to all global and redshift-instantaneous quantities, including the SFRF and UVLF at different redshifts using the recent high-redshift data by the JWST and the previous HST low-redshift data.

It is worth noting that calibrating our models to a different τ value, $\tau = 0.0627^{+0.0050}_{-0.0058}$, as recently determined by de Belsunce et al. (2021), and to the updated measurements of $\dot{N}_{\rm ion}$, presented by Becker et al. (2021), does not alter our findings. In summary, our results demonstrate that it is entirely possible to reproduce both cosmic dawn and reionization constraints with faint galaxy-dominated models without requiring new physics or exotic sources because our models with deduced parameters align well with the star formation efficiencies and timescales that have been reported in the literature. Our results shed additional light on the roles of faint and bright galaxies during cosmic dawn and reionization, which can be tested by upcoming JWST surveys.

Acknowledgments

The authors acknowledge insightful discussions with Adam Lidz, Tirthankar Roy Choudhury, Guochao Sun, Greg Bryan, Romain Teyssier, Lars Hernquist, Hy Trac, Matt Orr, Ulrich Steinwandel, Shy Genel, Francisco Villaescusa-Navarro, Kanan Datta, Saumyadip Samui, and Ken Van Tilburg, which have improved the paper significantly. We thank the anonymous referee for the comments that have improved the paper quality greatly. A.B. acknowledges financial support from the University Grant Commission (UGC), Govt. of India as a senior research fellow. A large fraction of this work has been done at CCA, Flatiron Institute, and A.B. and S.H. acknowledge support provided by the Simons Foundation. S.H. also acknowledges support for Program number HST-HF2-51507 provided by NASA through a grant from the Space Telescope Science Institute, which is operated by the Association of Universities for Research in Astronomy, incorporated, under NASA contract NAS5-26555. This work also used the Extreme Science and Engineering Discovery Environment (XSEDE), which is supported by National Science Foundation grant number ACI-1548562, and computational resources (Bridges) provided through the allocation AST190009.

ORCID iDs

Ankita Bera https://orcid.org/0000-0001-7072-570X
Sultan Hassan https://orcid.org/0000-0002-1050-7572
Aaron Smith https://orcid.org/0000-0002-2838-9033
Renyue Cen https://orcid.org/0000-0001-8531-9536
Enrico Garaldi https://orcid.org/0000-0002-6021-7020
Rahul Kannan https://orcid.org/0000-0001-6092-2187
Mark Vogelsberger https://orcid.org/0000-0001-8593-7692

References

Barkana, R. 2018, Natur, 555, 71
Barkana, R., & Loeb, A. 2001, PhR, 349, 125
Becker, G. D., & Bolton, J. S. 2013, MNRAS, 436, 1023
Becker, G. D., D'Aloisio, A., Christenson, H. M., et al. 2021, MNRAS, 508, 1853
Becker, G. D., Davies, F. B., Furlanetto, S. R., et al. 2018, ApJ, 863, 92
Bouwens, R. J., Illingworth, G. D., Oesch, P. A., et al. 2015, ApJ, 803, 34
Bowman, J. D., Rogers, A. E. E., Monsalve, R. A., Mozdzen, T. J., & Mahesh, N. 2018, Natur, 555, 67
Bradley, R. F., Tauscher, K., Rapetti, D., & Burns, J. O. 2019, ApJ, 874, 153
Carucci, I. P., & Corasaniti, P.-S. 2019, PhRvD, 99, 023518
Chabrier, G. 2003, PASP, 115, 763
Davies, F. B., Hennawi, J. F., Bañados, E., et al. 2018, ApJ, 864, 142
de Belsunce, R., Gratton, S., Coulton, W., & Efstathiou, G. 2021, MNRAS, 507, 1072
de Lera Acedo, E. 2019, in 2019 Int. Conf. on Electromagnetics in Advanced Applications (ICEAA) (Piscataway, NJ: IEEE), 0626
de Lera Acedo, E., de Villiers, D. I. L., Razavi-Ghods, N., et al. 2022, NatAs, 6, 984
DeBoer, D. R., Parsons, A. R., Aguirre, J. E., et al. 2017, PASP, 129, 045001
Ewall-Wice, A., Chang, T. C., Lazio, J., et al. 2018, ApJ, 868, 63
Ewall-Wice, A., Chang, T.-C., & Lazio, T. J. W. 2020, MNRAS, 492, 6086
Fan, X., Narayanan, V. K., Lupton, R. H., et al. 2001, AJ, 122, 2833
Feng, C., & Holder, G. 2018, ApJL, 858, L17
Fialkov, A., & Barkana, R. 2019, MNRAS, 486, 1763
Finlator, K., Davé, R., & Özel, F. 2011, ApJ, 743, 169
Finlator, K., Keating, L., Oppenheimer, B. D., Davé, R., & Zackrisson, E. 2018, MNRAS, 480, 2628
Finlator, K., Thompson, R., Huang, S., et al. 2015, MNRAS, 447, 2526
Foreman-Mackey, D., Hogg, D. W., Lang, D., & Goodman, J. 2013, PASP, 125, 306
Fraser, S., Hektor, A., Hütsi, G., et al. 2018, PhLB, 785, 159
Garaldi, E., Kannan, R., Smith, A., et al. 2022, MNRAS, 512, 4909
Gnedin, N. Y., Kravtsov, A. V., & Chen, H.-W. 2008, ApJ, 672, 765

Greig, B., Mesinger, A., & Bañados, E. 2019, MNRAS, 484, 5094
Hassan, S., Davé, R., Finlator, K., & Santos, M. G. 2016, MNRAS, 457, 1550
Hassan, S., Davé, R., Finlator, K., & Santos, M. G. 2017, MNRAS, 468, 122
Hills, R., Kulkarni, G., Meerburg, P. D., & Puchwein, E. 2018, Natur, 564, E32
Hoag, A., Bradač, M., Huang, K., et al. 2019, ApJ, 878, 12
Kannan, R., Garaldi, E., Smith, A., et al. 2022, MNRAS, 511, 4005
Katsianis, A., Blanc, G., Lagos, C. P., et al. 2017, MNRAS, 472, 919
Kaurov, A. A., & Gnedin, N. Y. 2014, ApJ, 787, 146
Kennicutt, R. C., Jr. 1998, ARA&A, 36, 189
Kulkarni, G., Keating, L. C., Haehnelt, M. G., et al. 2019, MNRAS, 485, L24
Ma, X., Kasen, D., Hopkins, P. F., et al. 2015, MNRAS, 453, 960
Madau, P. 2018, MNRAS, 480, L43
Madau, P., & Dickinson, M. 2014, ARA&A, 52, 415
Madau, P., & Fragos, T. 2017, ApJ, 840, 39
Madau, P., & Haardt, F. 2015, ApJL, 813, L8
Madau, P., Haardt, F., & Rees, M. J. 1999, ApJ, 514, 648
Madau, P., Pozzetti, L., & Dickinson, M. 1998, ApJ, 498, 106
Marinacci, F., Vogelsberger, M., Pakmor, R., et al. 2018, MNRAS, 480, 5113
Mason, C. A., Fontana, A., Treu, T., et al. 2019, MNRAS, 485, 3947
Mason, C. A., Treu, T., Dijkstra, M., et al. 2018, ApJ, 856, 2
McGreer, I. D., Mesinger, A., & D'Odorico, V. 2015, MNRAS, 447, 499
Mebane, R. H., Mirocha, J., & Furlanetto, S. R. 2020, MNRAS, 493, 1217
Mellema, G., Koopmans, L. V. E., Abdalla, F. A., et al. 2013, ExA, 36, 235
Mesinger, A., Aykutalp, A., Vanzella, E., et al. 2014, MNRAS, 446, 566
Mesinger, A., Furlanetto, S., & Cen, R. 2011, MNRAS, 411, 955
Mirocha, J., & Furlanetto, S. R. 2019, MNRAS, 483, 1980
Mittal, S., & Kulkarni, G. 2022, MNRAS, 515, 2901
Muñoz, J. B., Dvorkin, C., & Loeb, A. 2018, PhRvL, 121, 121301
Naiman, J. P., Pillepich, A., Springel, V., et al. 2018, MNRAS, 477, 1206
Nelson, D., Pillepich, A., Springel, V., et al. 2018, MNRAS, 475, 624
Ouchi, M., Shimasaku, K., Furusawa, H., et al. 2010, ApJ, 723, 869
Patil, A. H., Yatawatta, S., Koopmans, L. V. E., et al. 2017, ApJ, 838, 65
Pawlik, A. H., Schaye, J., & Dalla Vecchia, C. 2015, MNRAS, 451, 1586
Pillepich, A., Nelson, D., Hernquist, L., et al. 2018, MNRAS, 475, 648
Planck Collaboration, Aghanim, N., Akrami, Y., et al. 2020, A&A, 641, A6
Pospelov, M., Pradler, J., Ruderman, J. T., & Urbano, A. 2018, PhRvL, 121, 031103
Price, D. C., Greenhill, L. J., Fialkov, A., et al. 2018, MNRAS, 478, 4193
Robertson, B. E. 2022, ARA&A, 60, 121
Rosdahl, J., Blaizot, J., Katz, H., et al. 2022, MNRAS, 515, 2386
Schaerer, D. 2003, A&A, 397, 527
Sheth, R. K., & Tormen, G. 1999, MNRAS, 308, 119
Sims, P. H., & Pober, J. C. 2020, MNRAS, 492, 22
Singh, S., Jishnu, N. T., Subrahmanyan, R., et al. 2022, NatAs, 6, 607
Singh, S., & Subrahmanyan, R. 2019, ApJ, 880, 26
Slatyer, T. R., & Wu, C.-L. 2018, PhRvD, 98, 023013
Smit, R., Bouwens, R. J., Franx, M., et al. 2012, ApJ, 756, 14
Smith, A., Kannan, R., Garaldi, E., et al. 2022, MNRAS, 512, 3243
Sobacchi, E., & Mesinger, A. 2015, MNRAS, 453, 1843
Springel, V., & Hernquist, L. 2003, MNRAS, 339, 289
Springel, V., Pakmor, R., Pillepich, A., et al. 2018, MNRAS, 475, 676
Sun, G., & Furlanetto, S. R. 2016, MNRAS, 460, 417
Vogelsberger, M., Genel, S., Springel, V., et al. 2014a, Natur, 509, 177
Vogelsberger, M., Genel, S., Springel, V., et al. 2014b, MNRAS, 444, 1518
Vogelsberger, M., Marinacci, F., Torrey, P., & Puchwein, E. 2020, NatRP, 2, 42
White, R. L., Becker, R. H., Fan, X., & Strauss, M. A. 2003, AJ, 126, 1
Wise, J. H. 2019, arXiv:1907.06653
Wise, J. H., Demchenko, V. G., Halicek, M. T., et al. 2014, MNRAS, 442, 2560
Wu, X., McQuinn, M., & Eisenstein, D. 2021, JCAP, 2021, 042
Yeh, J. Y. C., Smith, A., Kannan, R., et al. 2023, MNRAS, 520, 2757
Zheng, Z., Cen, R., Trac, H., & Miralda-Escudé, J. 2011, ApJ, 726, 38